

Pulse sequences for controlled 2- and 3-qubit gates in a hybrid quantum register

Jingfu Zhang, Swathi S Hegde and Dieter Suter
 Fakultät Physik, Technische Universität Dortmund,
 D-44221 Dortmund, Germany
 (Dated: June 25, 2018)

We propose and demonstrate a quantum control scheme for hybrid quantum registers that can reduce the operation time, and therefore the effects of relaxation, compared to existing implementations. It combines resonant excitation pulses with periods of free precession under the internal Hamiltonian of the qubit system. We use this scheme to implement quantum gates like controlled-NOT operations on electronic and nuclear spins of the nitrogen-vacancy center in diamond. As a specific application, we transfer population between electronic and nuclear spin qubits and use it to measure the Rabi oscillations of a nuclear spin in a system with multiple coupled spins.

PACS numbers: 03.67.Pp, 03.67.Lx

I. INTRODUCTION

High precision quantum control is required in various fields, such as quantum computing [1–3]. The gate operations used for quantum control often rely on resonant electromagnetic fields that drive the targeted qubits near a resonant transition. While this drive operation should be strong, to dominate over unwanted effects and to allow short gate operations, the strength of the control field is often also limited by the requirement that it must not affect qubits that are not targeted in the specific operation.

Meeting these requirements becomes progressively more challenging as the number of qubits increases, as larger systems have more resonant transitions that must be considered. In many systems, the strengths of the couplings between the qubits, which are essential for multi-qubit gates, cover a significant range of values. If the couplings are weak, the duration of the gate operations that rely on these interactions, increases correspondingly. Multi-qubit operations often rely on transition selective pulses [4–8], which are designed to drive only a single transition with a resonant field. The condition that this field should be weak compared to the strength of the coupling constant may then be in conflict with the requirement that the gate operation should be fast compared to the relaxation time.

To avoid this conflict, we propose and demonstrate here an alternative approach, which is often used in liquid-state magnetic resonance but less frequently in solid-state systems like the diamond nitrogen-vacancy (NV) center [9]. It is based on combining hard pulses, i.e. driving fields that are strong compared to the couplings, with periods of free precession, where the coupling differentiates between the different qubit states. The resulting gate durations are the minimum possible for the given system. Compared to the approach with transition-selective pulses, this technique also offers the possibility to combine the pulses with techniques for reducing decoherence [10], such as dynamical decoupling. In particular, dynamical decoupling pulses can be combined with gate

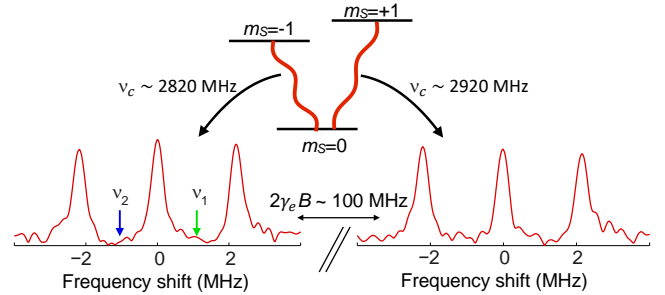


FIG. 1: (color online). Energy level system and spectra of the ESR transitions between the states with $m_S = 0$ and ∓ 1 , obtained as Fourier-transforms of time-domain signals. The origins of the frequency axes are set to $D \pm \gamma_e B$. The vertical arrows indicate the carrier frequencies $\nu_{1,2}$ for the MW pulses to implement the conditional operations U_1 and U_2 , respectively.

operations for designing gates that are protected against environmental noise [6, 11].

II. ELECTRON SPIN + ^{14}N NUCLEAR SPIN

A. Hamiltonian

The system that we consider consists of the electron spin and the ^{14}N nuclear spin system of a single NV center. If the magnetic field is oriented along the NV symmetry axis, the relevant Hamiltonian can be written as [9, 12]

$$\frac{1}{2\pi} \mathcal{H}_{E,N} = DS_z^2 - \gamma_e BS_z + PI_z^2 - \gamma_n BI_z + AS_z I_z. \quad (1)$$

Here S_z and I_z are z -components of the spin-1 operators for the electronic and nuclear spins, respectively. The zero-field splitting is $D = 2.87$ GHz, the nuclear quadrupolar splitting is $P = -4.95$ MHz, and the hyperfine coupling $A = -2.16$ MHz [12–14]. The electronic gyromagnetic ratio is $\gamma_e = -28$ GHz/T, and the nuclear gyromagnetic ratio $\gamma_n = 3.1$ MHz/T. In the experiments, the static field strength is about 1.8 mT, which

results in a separation of the two electron spin resonance (ESR) transitions by about 100 MHz. Figure 1 shows the spectra of the ESR transitions between the states with $m_S = 0$ and ∓ 1 , obtained in Ramsey-type free-induction decay (FID) time-resolved experiments, using resonant microwave pulses with Rabi frequencies of about 10 MHz for excitation and detection.

Since the experimental Rabi frequency is small compared to the separation of the two ESR transitions, the individual experiments are confined to a subspace of the full Hilbert space. We consider here the six-dimensional subspace spanned by the states

$$\{|0\rangle_e, |-1\rangle_e\} \otimes \{|1\rangle_n, |0\rangle_n, |-1\rangle_n\}, \quad (2)$$

which is associated to the ESR transition between $|0\rangle_e$ and $|-1\rangle_e$, with a transition frequency $D + \gamma_e B \sim 2820$ MHz. It thus contains one qubit (electron spin; target qubit) and one qutrit (^{14}N spin; control qutrit). The relevant Hamiltonian is then

$$\frac{1}{2\pi} \mathcal{H}_{E,N}^{eff} = \frac{\nu}{2} \sigma_z \otimes E_3 + \frac{A}{2} \sigma_z \otimes I_z, \quad (3)$$

written in the rotating frame at the carrier frequency ν_c of the microwave, where σ_z denotes the z -component of the Pauli matrix for the pseudo spin 1/2 of the electron spin in the space $\{|0\rangle_e, |-1\rangle_e\}$, E_3 the identity operator in 3 dimensions, and

$$\nu = (D + \gamma_e B) - \nu_c \quad (4)$$

is the effective transition frequency of the electron spin qubit in the rotating frame. In addition, the interaction representation also eliminates the quadrupole and Zeeman interactions of ^{14}N nuclear spin, which are irrelevant for the purpose of this work.

B. Unitary gate operations

The basic microwave (MW) pulse sequence for a controlled operation consists of two $\pi/2$ pulses with a $\pi/2$ relative phase shift, separated by a period τ of free precession, during which the hyperfine interaction causes differential precession, depending on the state of the nuclear spin. This pulse sequence is closely analogous to sequences used in nuclear magnetic resonance (NMR) quantum computing for implementing CNOT gates [15] and in electron-nuclear double resonance (ENDOR) for polarizing the nuclear spin [14]. In the above mentioned reference frame, the unitary operation generated by the pulse sequence is

$$\begin{aligned} U = & -\frac{i}{2\sqrt{2}} [(c_-(\sigma_z - iE_2) + c_+(\sigma_x + \sigma_y)) \\ & \otimes [\sin(\pi A\tau)] I_z \\ & + \frac{i}{2\sqrt{2}} [c_+(\sigma_z - iE_2) - c_-(\sigma_x + \sigma_y)] \\ & \otimes \{[\cos(\pi A\tau) - 1] I_z^2 + E_3\}, \end{aligned} \quad (5)$$

Input	Output of U_1	Output of U_2
0 1	-1 1	0 1
0 0	0 0	-1 0
0 -1	-1 -1	0 -1
-1 1	0 1	-1 1
-1 0	-1 0	0 0
-1 -1	0 -1	-1 -1

TABLE I: (color online). Output states m_S and m_I of U_1 and U_2 for the system consisting of one qubit (electron S ; target) and one qutrit (nuclear spin I ; control). global phase factors have been ignored. The states that are unchanged are shown in black in the results, the transformed states in blue (for U_1) and green (for U_2).

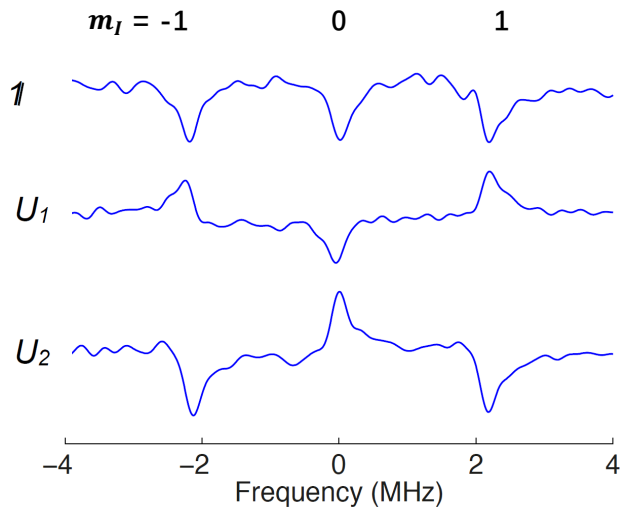


FIG. 2: (color online). Experimental ESR spectra obtained as Fourier-transforms of the FIDs, after applying the identity (top), U_1 (middle) and U_2 (bottom) gate operations. The quantum numbers above the spectra indicate the states of ^{14}N corresponding to the peaks.

with $c_{\pm} = \cos(\pi\nu\tau \pm \frac{\pi}{4})$. To obtain Eq. (5), we used

$$e^{-i\theta\sigma_z I_z} = -i \sin \theta \sigma_z I_z + [\cos \theta - 1] E_2 \otimes I_z^2 + E_2 \otimes E_3 \quad (6)$$

and assumed that the MW pulses are ideal, with duration zero.

When $\tau = 1/(2|A|)$, U corresponds to conditional qubit-qutrit operations, e.g. $U_1 = U(\nu_c \rightarrow \nu_1 = D + \gamma_e B - A/2)$ and $U_2 = U(\nu_c \rightarrow \nu_2 = D + \gamma_e B + A/2)$. Table I summarizes the effects of U_1 and U_2 on the basis states of the system. Up to some phase factors, they represent Controlled-NOT (CNOT) gates.

C. Experimental implementation

The experiments were performed at room temperature, using a diamond sample with natural abundance (1.1 %

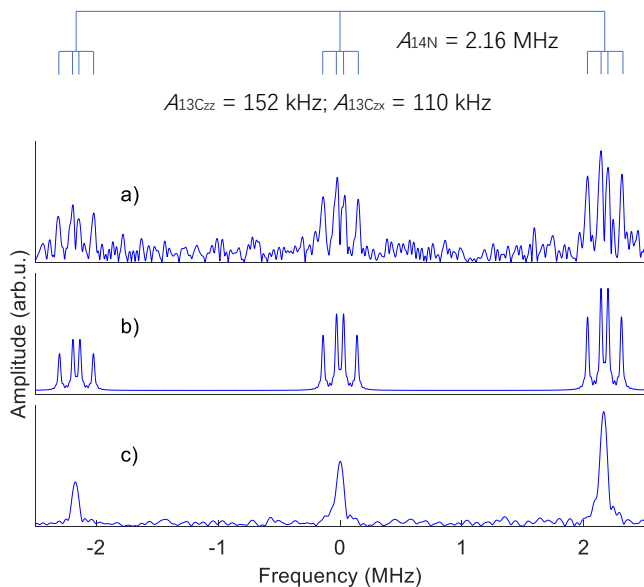


FIG. 3: (color online). Spectra of the electron spin coupled to one ^{14}N and one ^{13}C nucleus, obtained from an FID experiment (a) and the corresponding simulation (b). The origin of the frequency axis is $\nu_1 = D + \gamma_e B$. Due to the hyperfine coupling with the ^{13}C nucleus, each peak of the electron- ^{14}N system is split into four, shown by the schematic diagram at the top. The spectrum (c) was obtained from another electron spin which is only coupled to a ^{14}N .

^{13}C). The transverse relaxation time T_2^* of the electron spin was $\approx 2.5 \mu\text{s}$, measured in a Ramsey-type FID experiment. To test the sequence, we first initialized the electron spin of the NV center system into the $m_S = |0\rangle$ state by a laser pulse. To a first approximation, the nuclear spin is not affected by the laser pulse but remains unpolarized. Therefore the state of the two spins after the laser pulse is

$$\rho_{ini} = |0\rangle\langle 0| \otimes \frac{E_3}{3}, \quad (7)$$

where E_3 denotes the 3×3 unit operator. After the MW pulses, a second laser pulse measures the population of the $m_S = |0\rangle$ state. Figure 2 shows the experimental ESR spectra obtained as the Fourier-transforms of the FID. The uppermost trace shows the normal spectrum, i.e., without any gate operation; the second and third trace were obtained after applying the gates U_1 and U_2 . The signs of the peaks show that the electron spin states were inverted if the ^{14}N nuclear spin was in the $m_I = \pm 1$ state (for U_1) or in the $m_I = 0$ state (for U_2), as expected from table I.

III. ELECTRON, ^{14}N AND ^{13}C

As one example of the conditional gate operation U_2 , we use it for selective population transfer between the electronic and nuclear spins in a three-spin system consisting

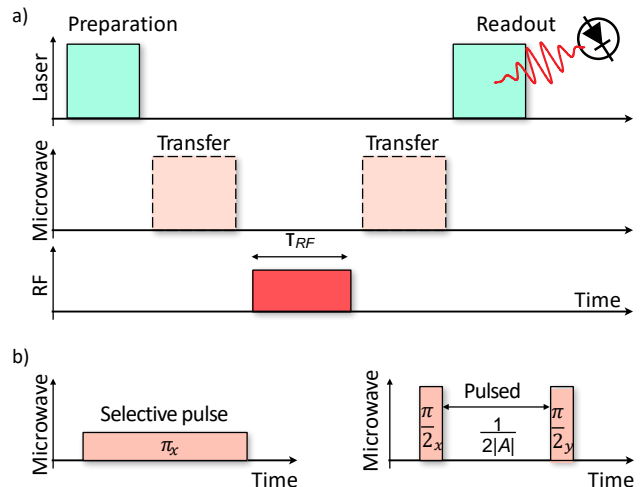


FIG. 4: (color online). (a) Pulse sequence for measuring Rabi frequency of the nuclear spin. The carrier frequency of the RF pulse is resonant with an NMR transition. The first transfer operation polarizes the nuclear spin, and the second acts as a readout to measure the remaining population after the RF pulse. (b) The MW pulse used for the population transfer in previous works (left) [16, 17], and in the present work (right). In the selective pulse method, the Rabi frequency of the MW pulse is about 0.2 MHz, while in pulsed transfer, the pulses are hard pulses with Rabi frequencies of about 10 MHz.

of the electron, the ^{14}N and one ^{13}C nuclear spin. Figure 3 (a) shows the spectrum of the electron spin, obtained from an FID experiment. The interaction with the ^{13}C nuclear spin splits each resonance line of the electron- ^{14}N spin system into four lines. This indicates that the strength of the hyperfine interaction of the ^{13}C is comparable to its nuclear Zeeman interaction, which is 165 kHz under our experimental conditions. Figure 3 (b) shows the simulated spectrum, with the couplings shown in the panel at the top of the figure.

An effective population transfer requires that the ^{14}N nuclear spin controls the evolution of the electron spin, with little perturbation from the ^{13}C spin. In our experiment, the coupling from the passive spin is not negligible, in contrast to previous experiments, where there was no passive spin [16], or the coupling from the passive spin was negligibly small compared to the active spin [17]. We first use the population transfer to polarise the ^{14}N nuclear spin, as shown in Figure 4. After the transfer, we measure the Rabi frequency of the ^{14}N spin by applying a constant radio-frequency (RF) field of variable duration τ_{RF} . After the RF pulse, we use another conditional gate operation for transferring the remaining nuclear spin polarisation back to the electron spin for detection.

The experiments were implemented in a ^{12}C enriched diamond sample, where decoherence due to ^{13}C nuclear spins is small and the coherence time of the electron spin is $\approx 20 \mu\text{s}$. To evaluate the effect of the passive ^{13}C , we compare two centers, one with and one without the ^{13}C . The NV axes of the two centers point in the same

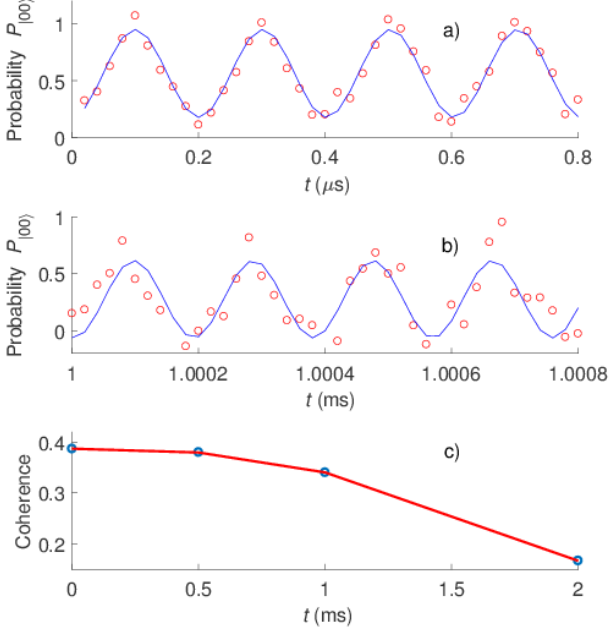


FIG. 5: (color online). Experiment results in estimating T_2^* time for ^{14}N . (a-b) The probability of state $|0,0\rangle$ measured in the FID experiments in various time period, where the measured data and fitting results are indicated by circles and solid curves respectively. (c) The coherence extracted from the FID experiments changes against time. By fitting the measured data shown as the circles using a function as $A_0 e^{-(t/T_2^*)^k}$, we can obtain $T_2^* = 2.1$ ms, $A_0 = 0.39$ and $k = 2.7$.

direction, and the NMR transition frequencies in the concerned subspace $\{m_S = |0\rangle, |-1\rangle\}$ for these two centers were 4.981, 4.905, 2.822, and 7.075 MHz, for the transitions between the states $|0,0\rangle \leftrightarrow |0,-1\rangle$, $|0,0\rangle \leftrightarrow |0,1\rangle$, $|-1,0\rangle \leftrightarrow |-1,-1\rangle$ and $|-1,0\rangle \leftrightarrow |-1,1\rangle$. Figure 3 (c) shows the spectrum obtained from the electron spin without a coupled ^{13}C . For both centers, we performed measurements with the two different transfer techniques. For estimating the T_2^* for ^{14}N , we used the standard pulse sequence to measure the FID of the ^{14}N [16, 17]. In the measurement, the MW and RF pulses were transition-selective, resonant with the transitions $|0,0\rangle \leftrightarrow |-1,0\rangle$ and $|0,0\rangle \leftrightarrow |0,-1\rangle$, respectively. We performed the experiments by choosing various time periods, and measuring the population of the state $|0,0\rangle$. Figure 5 shows the experimental results. Through fitting the coherence extracted from the series FID experiments, we can obtain $T_2^* = 2.1$ ms. Since this value is close to the longitudinal relaxation time T_1 of the electron spin, which was measured as ≈ 3.5 ms, the precision of this strategy is limited by the T_1 value of the electron.

We firstly applied the pulse sequence used in the previous works to a center without coupled ^{13}C . The Rabi frequency of the MW pulses was 0.19 MHz, with the

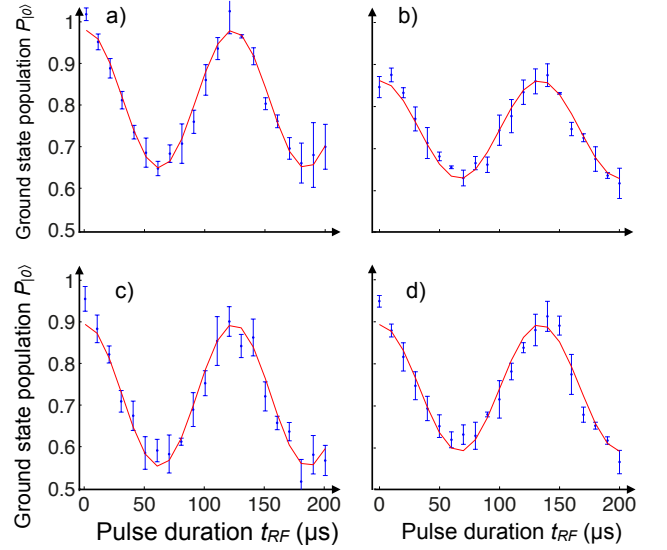


FIG. 6: (color online). Results of ^{14}N Rabi experiments in the NV centers without and with coupled ^{13}C , shown as left and right columns, from previous (top) and the new sequence proposed here (bottom).

carrier frequency set to the transition between the $|0,0\rangle$ and $|-1,0\rangle$ states. The frequency of the RF pulse was 4.981 MHz. The experimentally measured Rabi nutation is shown in Figure 6 (a), together with a fit to the function

$$P_{|0\rangle} = \alpha + \beta \cos(2\pi\nu_R t_{RF}), \quad (8)$$

where ν_R denoted the measured Rabi frequency for ^{14}N , and α and β are two constant. Table II shows the parameter values obtained by fitting the experimental data. Here we chose Figure 6 (a) as a reference for evaluating the following experiments.

Figure 6 (b) shows the results obtained in the center coupled with ^{13}C , from the previous pulse sequence in Figure 4, where the Rabi frequency of the two MW pulses is 0.21 MHz. By comparing with Figure 6 (a), one can find that the signal was degraded by the couplings from ^{13}C , shown as the loss of the strength of the signal by 12% and the decrease of the amplitude of the oscillation as 29%, since the Rabi frequency of the MW pulses is not large enough compared with the splitting caused by ^{13}C , which is about 0.15 MHz.

Figure 6 (c-d) shows the results obtained from our modified sequence shown in Figure 4, applied to the centers without and with the coupled ^{13}C . Table II shows the fitted parameters. Comparing the values for (d) and (b) shows a significant advantages for the new pulse sequence, which increases the oscillation amplitude of the signal by 21%. This advantages can be traced to the reduced effect of the coupling to ^{13}C due to the faster operations. One can estimate that the infidelity caused by the coupling from ^{13}C can be reduced by $\sim A/\nu_{1,MW} > 10$, where $\nu_{1,MW} = 0.21$ MHz is the Rabi frequency of the

	α	β	ν_R (kHz)
Fig. (a)	0.816	0.164	8.2
Fig. (b)	0.743	0.117	7.5
Fig. (c)	0.723	0.168	8.1
Fig. (d)	0.742	0.151	7.5

TABLE II: Fit results from the experiment data shown in Figures 6 (a-d).

transition selective MW π pulses in Figure 4.

IV. CCNOT GATE

^{13}C nuclear spins close to NV centers are interesting candidates for qubits [18], provided effective gate operations can be implemented. If the hyperfine coupling is strong, 2-qubit gates can be implemented by transition-selective pulses [17]. However, if multiple qubits are required, such as for the implementation of quantum error correction, it also becomes important to control more remote ^{13}C spins [19, 20]. In these cases, selective pulses result in long gate times and as a result, the coherence time of the electron spin limits the fidelity of the overall gate operation. The pulsed scheme discussed above results in significantly shorter gate times and can thus alleviate this problem.

In this section, we still consider a system consisting of one electron, one ^{14}N and one ^{13}C spin. We implement CNOT in the electron- ^{13}C system, with the additional constraint that the ^{14}N nuclear spin is in the state $m_I = 1$. In the three spin system, this operation is a controlled-controlled NOT (CCNOT) gate, or Toffoli gate[2], where ^{13}C and ^{14}N are the control spins, and the electron spin is the target. Since our scheme to implement the CNOT relies only on the secular component A_{zz} of the hyperfine interaction, we choose a center for which the quantization axis is close to the NV-axis [21]. By aligning the field along the NV- axis, we can approximate the relevant interaction Hamiltonian between electron and ^{13}C as

$$\frac{1}{2\pi}\mathcal{H}_c = A_{zz}S_zs_z, \quad (9)$$

where s_z denotes the z -component of the ^{13}C nuclear spin operator.

We still use the ^{12}C enriched sample mentioned in the previous section, and perform the experiments at room temperature. The time T_2^* is about 10 μs . Figure 7 (a-b) shows the electron spin spectra obtained through FID measurements in the $m_S = 0$ and $m_S = \pm 1$ manifolds, respectively. The number of resonance lines indicates that in this center, the hyperfine tensor component A_{zx} is sufficiently small to be neglected (< 50 kHz). The splitting of the peaks indicates that $A_{zz} \approx 150$ kHz. In the following, we consider 2 subspaces of the full Hilbert space, both of which correspond to two-qubit systems with one

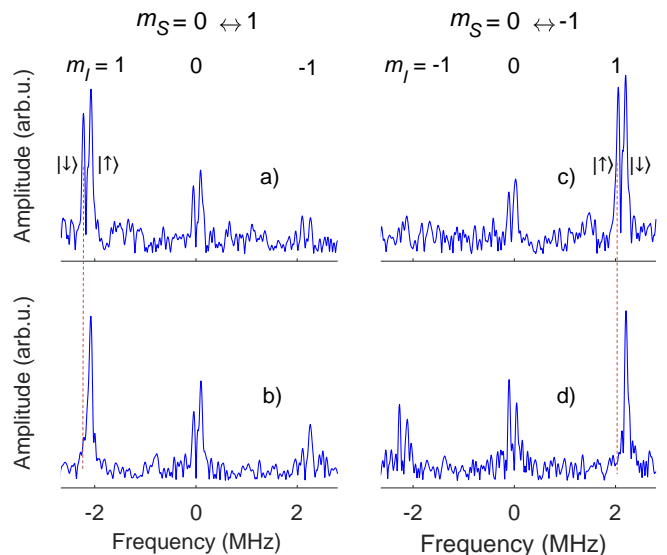


FIG. 7: (color online). Spectra of the electron spin coupled to one ^{14}N and one ^{13}C nucleus. The spectra in (a) and (c) are obtained from FIDs using MW pulses with the carrier frequencies set to the transition frequencies between states $m_S = 0$ and ± 1 , and Rabi frequencies of 6 and 10 MHz, respectively. The spectra in (b) and (d) show the results obtained from the FID after the CNOT gates were implemented in the $m_S = 0$ and ∓ 1 manifolds with ^{14}N in state $m_I = 1$, respectively. The states of the ^{13}C nuclear spin are indicated by \uparrow, \downarrow . The origin of the frequency axis in (a-b) is $D - \gamma_e B$, and in (c-d) $D + \gamma_e B$. The dashed vertical lines indicate the positions of resonance lines where the nuclear spins are in the state that corresponds to the control condition: in this case, the gate operation flips the electron spin, which is verified by the fact that the corresponding peaks are absent in the spectra (b) and (d).

Input	Output of CNOT ₁	Output of CNOT ₂
1 \uparrow	1 \uparrow	0 \uparrow
1 \downarrow	1 \downarrow	1 \downarrow
0 \uparrow	0 \uparrow	1 \uparrow
0 \downarrow	-1 \downarrow	0 \downarrow
-1 \uparrow	-1 \uparrow	-1 \uparrow
-1 \downarrow	0 \downarrow	-1 \downarrow

TABLE III: Output states electron (target) and ^{13}C (control) spins of the CNOT operations in the $m_S = 0$ and ∓ 1 manifolds, indicated as CNOT₁ and CNOT₂.

electron-spin qubit and one ^{13}C nuclear spin qubit, while the ^{14}N nuclear spin is in the $m_N = 1$ state. The first subspace is spanned by the states $m_S = 0$ and $m_S = -1$ of the electron and the second by the states $m_S = 0$ and $m_S = 1$. In these two subspaces, we implement two slightly different CNOT gates, with the electron spin as a target and the nuclear spin as the control qubit. In the first subspace, we use the control condition that the ^{13}C spin is in the \downarrow state, in the second subsystem that it is

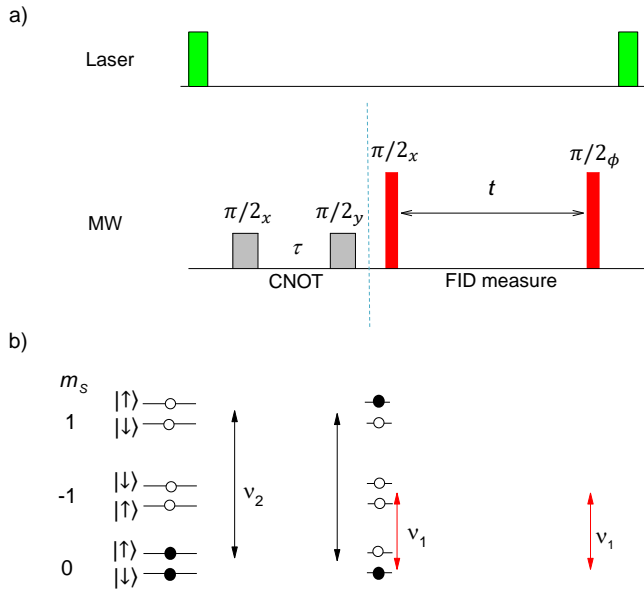


FIG. 8: (color online). (a) Pulse sequence for demonstrating the CNOT gate implemented in the electron- ^{13}C system. (b) Populations of the initial and final states when the CNOT gate is applied to subspace with $m_S = 0 \leftrightarrow -1$, $m_I = 1$. We therefore do not consider the ^{14}N states here. The filled and empty circles denote population of $1/2$ and 0 , respectively. The states marked by $|\uparrow\rangle$ and $|\downarrow\rangle$ are the ^{13}C eigenstates. The carrier frequencies of the MW pulses are set to the transition frequencies between $m_S = 0$ and 1 or -1 , indicated as the lines with double arrows. ν_1 and ν_2 indicate the transition frequencies $D \pm \gamma_e B$, respectively. The Rabi frequencies of the MW pulses are 0.5 and 10 MHz in the CNOT gate and the FID measurement, respectively.

in the state \uparrow . Table III summarises these gates.

Figure 8 shows the pulse sequence used. The double arrows indicate the carrier frequencies of the MW pulses. The Rabi frequency of the pulses in the CNOT is 0.5 MHz. These two pulses are as hard pulses for the electron and ^{13}C system, since the Rabi frequency is much larger than the coupling to ^{13}C , while they are selective with respect to the state of the ^{14}N . In order to observe the effects of the CNOT gate, we measured the FID signal. Figure 7 (c-d) shows the spectra of the electron after the implementation of the CNOT gates in the $m_S = 0$ and $m_S = \mp 1$ manifolds, respectively. The single peak in the left or right transition of the ^{14}N multiplet verifies the operation of the CNOT gate, which transfers population from states $|0\downarrow\rangle$ to $|-1\downarrow\rangle$, or $|0\uparrow\rangle$ to $|1\uparrow\rangle$, respectively. We use the amplitude ratio between the single peak and the corresponding peak in the doublet to estimate the fidelity of the CNOT gate, and obtained values of 0.99 and 0.95 for b) and d), respectively.

If we use a transition-selective pulse to implement the CNOT gate, its Rabi frequency may not exceed 20 kHz if the theoretical fidelity should be at least 0.99 in the absence of dephasing effects. For such a low Rabi fre-

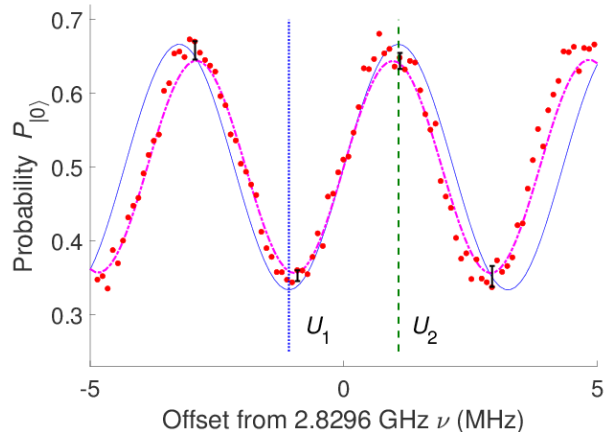


FIG. 9: (color online). Dependence of the operation U defined by Eq. (5) on the MW carrier frequency. The filled circles represent the experimental data, the full curve represents a simulation for ideal (δ -function) pulses, while the dash-dotted line was simulated with the pulse durations of $21.6 \mu\text{s}$ used in the experiment. The blue dotted vertical line indicates the offset used for implementing U_1 and the dark green dashed line for U_2 . The error bars represent the standard deviation of the measured data points.

quency, the duration of the π pulse becomes at least $25 \mu\text{s}$, which is longer than the relaxation time $T_2^* \approx 10 \mu\text{s}$. Dephasing would thus reduce the fidelity of such a gate operation to ~ 0.6 .

V. OFFSET DEPENDENCE

A. Narrow frequency range

The operations implemented by the $(\pi/2)_x - 1/2|A| - (\pi/2)_y$ pulse sequence depend strongly on the MW carrier frequency used to generate the pulses, as evidenced by the expression for U in Eq. (5). We therefore measured this dependence in the system consisting of the electron and ^{14}N nuclear spins as a function of the carrier frequency and measuring the resulting ground state population. Applying the unitary of Eq. (5) to the initial state (7) yields ground state population

$$P_{|0\rangle} = \frac{1}{2} - \frac{1}{6} \sin\left(\frac{\pi\nu}{A}\right). \quad (10)$$

Figure 9 shows the results of this experiment: The vertical axis represents the population of the $m_S = 0$ state measured by the second laser pulse as a function of the MW carrier frequency ν . The dotted and dashed vertical lines indicate the offsets where the operation corresponds to U_1 and U_2 , respectively. We compare the experimental results (filled circles) to a simulation of the experiment without dephasing effects, i.e. $T_2 \rightarrow \infty$, and using ideal pulses with infinite Rabi frequency of the MW

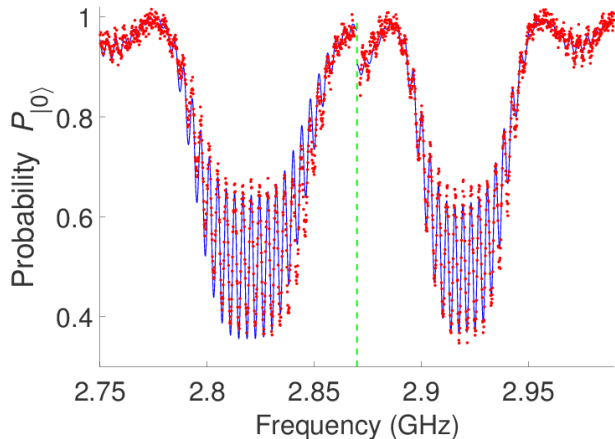


FIG. 10: (color online). Offset dependence of a CNOT gate with ^{14}N as the results in experiment and by simulation where the electron and ^{14}N spins are both treated as spin-1 systems, indicated by the filled dots and the solid curves, respectively. The horizontal axis shows the carrier frequency of the MW. We use two experiments by separating the scan into two segments, indicated by the dashed line, since the measured the Rabi frequencies at the transition frequencies are different.

pulses, shown as the full curve. The dash-dotted curve in the figure shows the result of a simulation for the actual Rabi frequency (11.6 MHz) used in the experiment, and $T_2 \rightarrow \infty$. It agrees well with the experimental data, indicating that T_2 effects are negligible in this experiment.

B. Wide frequency range

In addition to the data shown in Figure 9, we also measured the offset dependence over the whole frequency range from 2.75 to 2.99 GHz, to obtain the full offset dependence. Figure 10 shows the experimental results and compares them to a simulation that treats the nuclear and the electronic spins as spin-1 systems. Since the MW power at the sample varies as a function of frequency, we performed the experiment in two parts and set the duration of the $\pi/2$ pulses to $21.6 \mu\text{s}$ in the low-frequency part and to $27.5 \mu\text{s}$ in the high-frequency part. The two parts are separated by the dashed vertical line in figure 10. The agreement between theory and experiment is best near 2.83 GHz and 2.93 GHz, where the calibration for the pulse duration was performed.

C. Transition-selective pulse

For comparison, we also implemented U_2 in the conventional way [5–8], using one low power pulse with a Rabi frequency of 0.23 MHz. Figure 11 show the experimental and simulated results. The comparison between the experimental and simulated data shows that the T_2 effects cause $\sim 17\%$ loss of the fidelity of the gate, which

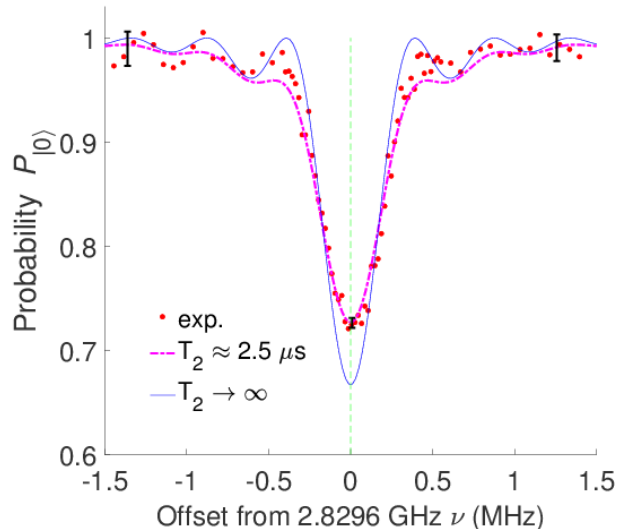


FIG. 11: (color online). Experimental results from a CNOT gate using a low-power pulse with a Rabi frequency of 0.23 MHz shown as circles. The dash-dotted and full curves show numerical simulations for the cases of $T_2 \approx 2.5 \mu\text{s}$ and $T_2 \rightarrow \infty$. The dashed vertical line indicates the offset for implementing U_2 .

is implemented at offset 0.

VI. CONCLUSIONS

The method for implementing CNOT gate based on transition-selective pulse is an approximation [4], and the fidelity is limited by the spectral resolution of the system. Our results show that these limitations can be circumvented by using quantum gates based on hard pulses and free precession periods. The resulting gate duration is considerably shorter, which reduces the effects of relaxation. In our experiments, we can implement a CNOT gate within 300 ns in the electron and nitrogen system, which is shorter than the pulse obtained by optimal control (~ 450 ns) [22], and much shorter than the transition-selective pulse ($1.8 \mu\text{s}$) [6]. The advantages were enhanced in the electron and ^{13}C system with the small coupling strength, e.g., about 150 kHz, where the spectral resolution seriously limits the fidelity of gates based on transition-selective pulses.

In conclusion, this new scheme for multi-qubit operations provides significant improvements for quantum registers consisting of electronic and nuclear spins. The benefits include reducing the gate time, and improving the control in the system with more couplings. The gates that we have chosen to implement here are important since they are members of the sets of gates required for universal quantum computing. Although we implemented the experiments in the NV center system, the method is completely general and can be applied to many other

systems.

VII. ACKNOWLEDGEMENT

This work was supported by the DFG through grant SU 192/34-1.

-
- [1] C. Brif, R. Chakrabarti and H. Rabitz, *New J. Phys.* **12**, 075008 (2010).
- [2] M. A. Nielsen and I. L. Chuang, *Quantum Computation and Quantum Information* (Cambridge University Press, Cambridge, 2000).
- [3] J. Stolze and D. Suter, *Quantum Computing: A Short Course from Theory to Experiment* (Wiley-VCH, Berlin, 2nd edition, 2008).
- [4] D. G. Cory, A. E. Dunlop, T. F. Havel, S. S. Somaroo, and W. Zhang, *Concepts Magn. Reson. Part A* **23**, 49 (2004).
- [5] F. Jelezko, T. Gaebel, I. Popa, M. Domhan, A. Gruber, and J. Wrachtrup, *Phys. Rev. Lett.* **93**, 130501 (2004).
- [6] J. Zhang and D. Suter, *Phys. Rev. Lett.* **115**, 110502 (2015).
- [7] M. Hirose and P. Cappellaro, *Nature* **532**, 77 (2016).
- [8] L. Robledo, L. Childress, H. Bernien, B. Hensen, P. F. A. Alkemade, and R. Hanson, *Nature* **477**, 574 (2011).
- [9] D. Suter and F. Jelezko, *Progress in Nuclear Magnetic Resonance Spectroscopy* **98-99**, 50 (2017).
- [10] D. Suter and G. A. Alvarez, *Rev. Mod. Phys.* **88**, 041001 (2016).
- [11] J. Zhang, A. M. Souza, F. D. Brandao, and D. Suter, *Phys. Rev. Lett.* **112**, 050502 (2014).
- [12] C. S. Shin, M. C. Butler, H.-J. Wang, C. E. Avalos, S. J. Seltzer, R.-B. Liu, A. Pines, and V. S. Bajaj, *Phys. Rev. B* **89**, 205202 (2014).
- [13] X.-F. He, N. B. Manson, and P. T. H. Fisk, *Phys. Rev. B* **47**, 8816 (1993).
- [14] B. Yavkin, G. Mamin, and S. Orlinskii, *J. Magn. Reson.* **262**, 15 (2016).
- [15] I. Chuang, N. Gershenfeld, M. Kubinec, and D. Leung, *Proc. Roy. Soc. Lond. A* **454**, 447 (1998).
- [16] T. van der Sar, Z. H. Wang, M. S. Blok, H. Bernien, T. H. Taminiau, D. M. Toyli, D. A. Lidar, D. D. Awschalom, R. Hanson, and V. V. Dobrovitski, *Nature* **484**, **82** (2012).
- [17] J. H. Shim, I. Niemeyer, J. Zhang, and D. Suter, *Phys. Rev. A* **87**, 012301 (2013).
- [18] J. Wrachtrup, S. Y. Kilin, and A. P. Nizovtsev, *Optics and Spectroscopy* **91**, 429 (2001).
- [19] G. Waldherr, Y. Wang, S. Zaiser, M. Jamali, T. Schulte-Herbrueggen, H. Abe, T. Ohshima, J. Isoya, J. F. Du, P. Neumann, et al., *Nature* **506**, 204 (2014).
- [20] T. H. Taminiau, J. Cramer, T. van der Sar, V. V. Dobrovitski, and R. Hanson, *Nature Nanotechnology* **9**, 171 (2014).
- [21] A. Dreau, P. Spinicelli, J. R. Maze, J.-F. Roch, and V. Jacques, *Phys. Rev. Lett.* **110**, 060502 (2013).
- [22] J. Geng, Y. Wu, X. Wang, K. Xu, F. Shi, Y. Xie, X. Rong, and J. Du, *Phys. Rev. Lett.* **117**, 170501 (2016).